Article | Open Access

Energy Materials

Kang et al. Energy Mater. 2026, 6, 600090 DOI:10.20517/energymater.2026.129

Mitigating hydrogen evolution via ionomer structure for efficient CO_2 reduction in acidic membrane electrode assembly electrolyzers

Zhongyin Kang[1,2], Min Zhang[1,2], Yang Wang[1,2], Qiang Liao[1,2], Qian Fu[1,2,*], Xun Zhu[1,2,*]

Keywords:
Acidic CO_2 reduction, ionomer structure, interfacial microenvironment, hydrogen-bond network, membrane electrode assembly

Citation: Kang, Z.; Zhang, M.; Wang, Y.; Liao, Q.; Fu, Q.; Zhu, X. Mitigating hydrogen evolution via ionomer structure for efficient CO_2 reduction in acidic membrane electrode assembly electrolyzers. *Energy Mater.* **2026**, *6*, 600090. https://dx.doi.org/10.20517/energymater.2026.129

Received: 19 May 2026
First Decision: 9 Jun 2026
Revised: 30 Jun 2026
Accepted: 17 Jul 2026
Published: 31 Jul 2026

Academic Editor: Ho Won Jang
Copy Editor: Fangling Lan
Production Editor: Fangling Lan

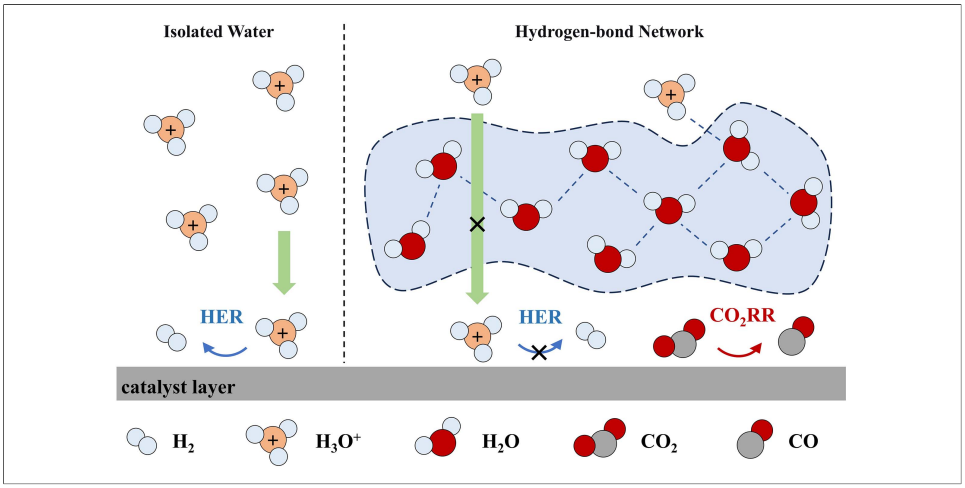

Abstract

Electrocatalytic CO_2 reduction in acidic media suppresses (bi)carbonate formation and improves CO_2 single-pass conversion, but the catalyst layer in contact with the hydrated proton environment usually leads to severe competing hydrogen evolution reaction (HER). Regulating the interfacial microenvironment is an effective strategy to inhibit the migration of H^+ during the electrolysis process and block the contact between H_2O and the catalyst. In this work, we systematically investigate the influence of ionomer side chain on the interfacial water structure in an acidic membrane electrode assembly electrolyzer. The short side chain ionomer D79, characterized by a high density of sulfonic acid groups, generates abundant nanoscale micropores and promotes a more ordered dipole alignment of water molecules. *In situ* attenuated total reflection surface-enhanced infrared absorption spectroscopy reveals that over 60% of the interfacial water exists as strongly hydrogen-bonded water on the catalyst surface under an applied potential, which is conducive to suppressing HER from protons and free water. Optimizing the ionomer ratio to 20 wt% balances CO_2 transport and hydrated proton migration. Consequently, the D79-modified electrode achieves a CO Faradaic efficiency (FE_{CO}) of 91.1% at 500 mA cm^{-2}, significantly

[1]Key Laboratory of Low-Grade Energy Utilization Technologies and Systems, Ministry of Education, Chongqing University, Chongqing 400044, China.
[2]Institute of Engineering Thermophysics, School of Energy and Power Engineering, Chongqing University, Chongqing 400044, China.

*Correspondence to: Prof. Qian Fu, Prof. Xun Zhu, Institute of Engineering Thermophysics, School of Energy and Power Engineering, Chongqing University, Chongqing 400044, China. E-mail: fuqian@cqu.edu.cn; zhuxun@cqu.edu.cn

outperforming most reported studies. This work demonstrates that ionomer side chains can effectively regulate the hydrogen-bond network and suppress competitive HER, offering critical insights into interfacial microenvironment engineering for acidic CO_2 electrolysis.

INTRODUCTION

The CO_2 reduction (CO_2RR) represents a promising strategy for converting carbon emissions into valuable chemicals and fuels, making a significant contribution towards achieving carbon neutrality[1-4]. Numerous previous studies have primarily focused on CO_2RR in alkaline media, as the alkaline environment suppresses the competing HER and enables high product selectivity. However, in alkaline media, CO_2 readily reacts with OH^- to form (bi)carbonate species ($CO_2 + 2OH^- \rightarrow CO_3^{2-} + H_2O$, $CO_2 + OH^- \rightarrow HCO_3^-$), which migrate across the membrane toward the anode during electrolysis, limiting the single-pass conversion efficiency of CO_2[5,6]. To achieve a higher single-pass conversion, acidic media have been proposed as an alternative. In acidic environments, once (bi)carbonate is formed, it is rapidly reconverted to CO_2 by the abundant H^+ ($CO_3^{2-} + 2H^+ \rightarrow CO_2 + H_2O$, $HCO_3^- + H^+ \rightarrow CO_2 + H_2O$), which has demonstrated potential in improving overall carbon efficiency [Supplementary Figure 1][7-9].

However, the acidic environment also intensifies the competitive HER, making it imperative to develop strategies that can selectively suppress the more kinetically favorable HER[10-12]. To date, adjusting the interfacial microenvironment in acid has proven to be an effective approach for suppressing the HER and improving product selectivity[13,14]. Recent studies have primarily focused on modulating the cathode interfacial microenvironment using alkali cations. Under an applied voltage, these positively charged alkali cations can form a local electric field on the electrode surface, which is in favor of repelling H^+ to suppress HER[15,16]. During the electrolysis process, however, alkali cations continuously accumulate at the catalyst surface. Once the (bi)carbonate species formed from CO_2RR-generated OH^- and CO_2 exceeds the buffering capacity of H^+, it precipitates as bicarbonate salts with alkali cations, rapidly clogging the electrodes and electrolyzer flow channels and leading to system deactivation[17,18]. Therefore, it is necessary to avoid strategies that increase cation concentration to inhibit HER.

The ionomer on the catalyst layer surface serves as a critical channel for proton and water transport[19]. By influencing the hydrogen-bonding network and interfacial water, the ionomer can regulate the local microenvironment and thereby suppress the HER[20]. During CO_2 electrolysis, H_3O^+ can continuously migrate from the anode to the cathode across the proton exchange membrane. Given that the kinetics of CO_2RR are slower than those of HER, both interfacial H_2O and H^+ serve as potential proton sources for reduction[21]. Therefore, improving the integrity of the interfacial hydrogen-bonding network is conducive to suppressing the consumption of free water and impeding the migration of H^+ toward the catalyst surface, thus enabling CO_2RR in acidic membrane electrode assembly (MEA) electrolyzers. Based on the difference in functional groups, ionomers are classified into anion-exchange ionomers (AEI) and cation-exchange ionomers (CEI). AEI represented by Sustainion are susceptible to functional group degradation under strongly acidic conditions and thus lose their functionality, rendering CEI the only viable choice in acidic systems[22]. Nafion is the most widely applied CEI; however, the conventional long-side-chain Nafion (e.g., D520, with a side chain of approximately 6 to 7 atoms) exhibits structural deficiencies in acidic CO_2 electrolysis. Its flexible long side chains lead to excessively wide ion-cluster channels (> 2.5 nm), providing insufficient sieving of hydronium ions. A substantial flux of H^+ reaches the catalyst surface and neutralizes the local high-pH microenvironment, allowing HER to dominate. Meanwhile, the sparse distribution of sulfonic acid groups limits its capacity to regulate the interfacial water structure[23]. The short side chain (SSC) Aquivion (e.g., D79, with a side chain approximately one-third the length of the former) addresses these issues. The narrowed ion-cluster channels (approximately 1.5 nm) effectively block hydronium ions,

while the denser distribution of sulfonic acid groups facilitates the reinforcement of the hydrogen-bonding network for constraining interfacial water. Nevertheless, the quantitative correlation between side chain length and its impact on interfacial water structure, as well as CO_2RR performance, warrants further investigation.

In this study, we investigated the impact of the side chain on the interfacial water hydrogen-bond network for acidic CO_2RR. We focused on SSC ionomers, which feature a higher density of sulfonic acid groups, resulting in smaller micropores at the nanoscale. *In situ* attenuated total reflection surface-enhanced infrared absorption spectroscopy (ATR-SEIRAS) revealed that the higher density of sulfonic acid groups and micropores in the SSC ionomer led to a more ordered dipole alignment of water molecules, with over 60% of the interfacial water existing as strongly hydrogen-bonded water, which effectively suppressed the HER under high current densities in acidic media. Furthermore, *in situ* electrochemical impedance spectroscopy (EIS) and distribution of relaxation times (DRT) analysis showed that tuning the ionomer ratio optimized the CO_2 transport, achieving a FE_{CO} of 91.1% at 500 mA cm^{-2}, significantly outperforming most reported studies [Supplementary Table 1]. Overall, this work offers critical insights into the regulation of the interfacial microenvironment by ionomer structure and loading for acidic CO_2RR in MEA electrolyzers.

EXPERIMENTAL

Preparation of catalyst and gas diffusion electrodes

We synthesized the Ni-N-C catalyst through a high-temperature pyrolysis route using carbon black as the support material. Typically, nickel(II) acetate (3.6 mg, Macklin) and 1,10-phenanthroline monohydrate (8.5 mg, Macklin) were dissolved in anhydrous ethanol (2 mL), then ultrasonicated to obtain a homogeneous dispersion. Subsequently, Carbon black (10 mg) was introduced into the mixture and stirred at 80 °C for 8 h in a constant-temperature water bath. The resulting mixture was then placed in an oven and dried at 60 °C overnight to obtain a powder sample. Urea (Macklin) was subsequently introduced at a urea-to-sample mass ratio of 10:1, and the combined mixture was ground mechanically. The obtained powder was sequentially heat-treated at 600 °C for 2 h and then at 800 °C for 1 h. Thereafter, the product was washed with diluted hydrochloric acid (10 vol%) over 24 h, then collected by suction filtration and dried at ambient temperature for another 24 h to yield the final Ni-N-C catalyst.

Ni-N-C gas diffusion electrodes (GDEs) containing different ionomers were fabricated via ultrasonic spray deposition. The catalyst ink consisted of Ni-N-C catalyst (40 mg), D79 ionomer dispersion (35 μL, 25 wt%, Syensqo), and anhydrous ethanol (18 mL). This mixture was ultrasonicated for 30 min to ensure uniform dispersion, then sprayed onto a carbon paper substrate (3 × 3 cm^2, H15C13, Freudenberg) using an ultrasonic spray coater. The resulting GDE exhibited an ionomer content of 20 wt% and a catalyst loading of 2 mg cm^{-2}. GDEs containing different types of ionomers (D72, 25 wt%, Syensqo; D520, 5 wt%, DuPont; D521, 5 wt%, DuPont) and varying ionomer contents (5, 10, 20, 30 and 40 wt%) were fabricated following the same procedure. The anode consisted of a 2.5 × 2.5 cm^2 titanium felt with a thickness of 0.25 mm (coated with iridium, Fuershun Electronic Material Co., Jiangsu, China).

Materials characterization

Scanning electron microscopy (SEM) imaging was conducted using a Hitachi S-4800 microscope at an accelerating voltage of 3.0 kV, and energy-dispersive X-ray spectroscopy (EDS) maps were collected using the same instrument. High-angle annular dark-field scanning transmission electron microscopy (HAADF-STEM) imaging was performed on an FEI Tecnai G2 F20 microscope at an accelerating voltage of 200 kV. To investigate the microporous structure below 2 nm and CO_2 adsorption performance of the ionomers, the ionomer materials were characterized by CO_2 adsorption-desorption measurements. CO_2 adsorption-desorption measurements were performed using an ASAP 2460 analyzer (Micromeritics) at 0 °C. Prior to

measurement, approximately 100 mg of ionomer was degassed at 120 °C under vacuum for 12 h. The CO_2 adsorption isotherms were recorded in the relative pressure (P/P_0) range of 10^{-5} to 0.99. The specific surface area was determined using the Brunauer-Emmett-Teller (BET) method. Micropore size distribution was calculated using the density functional theory (DFT) model. CO_2 uptake capacity was determined from the adsorption amount at $P/P_0 \approx 0.95$. Water uptake of the ionomer materials was measured gravimetrically. Ionomer membranes (approximately 2 × 2 cm^2) were dried at 80 °C under vacuum for 24 h to obtain the dry weight (W_{dry}). The membranes were then immersed in deionized water at room temperature for 3 h to ensure complete hydration. The wet membranes were gently blotted with filter paper to remove surface water and immediately weighed (W_{wet}). The water uptake was calculated as: Water uptake (%) = (W_{wet} - W_{dry})/W_{dry} × 100%. Each measurement was repeated three times, and the average values are reported.

Electrochemical measurements

MEA electrolyzer test

The performance of CO_2 electrolysis under high current densities was evaluated using an acidic MEA electrolyzer [Supplementary Figure 2]. A 2.5 × 2.5 cm^2 titanium felt with a thickness of 0.25 mm (coated with iridium) served as the anode, while Ni-N-C GDEs containing various ionomers (1 × 1 cm^2) functioned as the cathode. A proton exchange membrane (PEM, Nafion 117, DuPont) was positioned between the two electrodes. The anode chamber received a continuous supply of 0.5 M K_2SO_4 electrolyte at 15 mL min^{-1} via a peristaltic pump, and its pH was set to 1 using H_2SO_4, whereas humidified CO_2 was supplied to the cathode chamber at 100 mL min^{-1}. Galvanostatic electrolysis was performed at current densities ranging from 100 to 500 mA cm^{-2}. Cyclic voltammetry (CV) was performed at scan rates of 10, 12, 14, 16, and 18 mV s^{-1} over the potential range of 0.1-0.2 V *vs.* reversible hydrogen electrode (RHE). The scan rates were varied to determine the electrochemical double-layer capacitance (C_{dl}) from the slope of the current density (at the midpoint potential) *vs.* scan rate plot. The C_{dl} value is proportional to the electrochemically active surface area (ECSA), enabling comparison of the accessible active surface area for GDEs modified with different ionomer ratios. Galvanostatic EIS measurements were performed in a MEA electrolyzer over a frequency range from 100 kHz to 1 Hz, with 10 data points acquired per decade and an amplitude of 10 mA. The EIS data were collected after a 5 min galvanostatic hold at the desired current density. For instance, prior to collecting the EIS spectrum at 100 mA cm^{-2}, the MEA electrolyzer was operated at 100 mA cm^{-2} for 5 min. To facilitate a more accurate interpretation of the EIS results, the DRT method was employed to extract the electrochemical processes corresponding to different time constants (e.g., charge transfer, diffusion, *etc.*) from the impedance data. Through mathematical transformation, the impedance response was converted into the relaxation time distribution function $\gamma(\tau)$, enabling the identification and quantification of the contribution of each process to the overall polarization.

In situ ATR-SEIRAS measurements

In situ ATR-SEIRAS measurements were conducted on a Bruker INVENIO FTIR spectrometer coupled to an electrochemical workstation. A three-electrode spectroelectrochemical cell with an ATR optical configuration was employed, wherein an Ag/AgCl electrode (saturated KCl) served as the reference electrode, a high-purity Pt wire as the counter electrode, and the as-prepared sample as the working electrode [Supplementary Figure 3]. The electrolyte consisted of CO_2-saturated 0.5 M K_2SO_4, acidified to pH 1 with H_2SO_4. Prior to and during the measurements, high-purity CO_2 was continuously purged through the electrolyte at a flow rate of 30 mL min^{-1} for at least 30 min to ensure saturation. All spectra were acquired over the wavenumber range of 4,000-400 cm^{-1}, and each spectrum was averaged from 32 scans at a spectral resolution of 8 cm^{-1}. All measured potentials were referenced to the RHE scale according to the formula: E (V *vs.* RHE) = E (V *vs.* Ag/AgCl) + 0.197 + 0.0591 × pH[23].

Product analysis

The gaseous products (CO and H_2) collected after electrolysis were analyzed by a gas chromatograph (GC) equipped with a flame ionization detector (FID) for CO and a thermal conductivity detector (TCD) for H_2.

The FE values for CO and H_2 were determined using the following equation[24]:

$$FE = n_i Z_i F/Q \times 100\%$$

where Z_i represents the number of electrons transferred per mole of product i (CO or H_2), F represents the Faradaic constant (96,485 C mol^{-1}), n_i (mol) denotes the molar quantity of product i produced, and Q (C) refers to the total charge quantity.

The partial current density (j_i) for each product was determined using the following equation[24]:

$$j_i = j_{total} \times FE_i$$

where j_{total} denotes the overall current density applied to the system, and FE_i is the Faradaic efficiency of product *i*.

Instruments and characterization equipment

The following instruments were used in this study: scanning electron microscopy (S-4800, Hitachi, Japan); high-angle annular dark-field scanning transmission electron microscopy (Tecnai G2 F20, FEI, USA); CO_2 adsorption-desorption measurements (ASAP 2460, Micromeritics, USA); gas chromatography (8890, Agilent Technologies, USA); electrochemical workstation (PARSTAT MC, Princeton Applied Research, USA); *in situ* ATR-SEIRAS (INVENIO, Bruker, Germany); ultrasonic spray coater (SimCoat Coating System, Sono-Tek, USA). All instruments were operated according to the manufacturers' specifications.

RESULTS AND DISCUSSION

Morphological and structural characterization

This study investigates the influence of ionomers on CO_2RR in an MEA-type electrolyzer. In the MEA, humidified CO_2 from the cathode flow channel is transported through the gas diffusion layer (GDL) to the catalyst, while anodic water concurrently crosses the membrane to reach the reaction interface. At the three-phase interface, CO_2, protons, and electrons are consumed to generate CO and H_2, rendering CO_2 transport and interfacial water structure critical determinants of MEA performance. Ni-N-C is selected as the catalyst due to its low cost as a non-precious metal catalyst and its excellent CO selectivity, making it widely adopted in this field. During the preparation of GDE, the catalyst ink is uniformly sprayed onto the GDL, forming a thin film of ionomer that encapsulates the carbon support and catalyst surface [Figure 1A]. The resulting cathode and anode are closely assembled with the membrane to form an MEA structure. As illustrated in Figure 1B, the ionomer consists of a hydrophobic polytetrafluoroethylene (PTFE) main chain and pendant side chains carrying terminal hydrophilic sulfonic acid groups (-SO_3H), which establish CO_2 and water transport channels, respectively, at the three-phase interface. The SSC ionomer features a SSC structure, namely -O-CF_2-CF_2-SO_3H, whereas the LSC ionomer possesses a longer side chain, -O-CF_2-$CF(CF_3)$-O-CF_2-CF_2-SO_3H. The shorter side chain of the SSC ionomer enables a higher density of sulfonic acid groups per unit polymer mass, which is corroborated by its higher ion-exchange capacity. The SSC ionomer, with its hydrophilic groups positioned closer to the backbone, exhibits lower ionomer-H_2O adsorption energy, enhanced acid resistance, improved water uptake, and higher proton conductivity, thereby promoting the formation of a unique interfacial water structure under acidic conditions[25]. To systematically investigate the

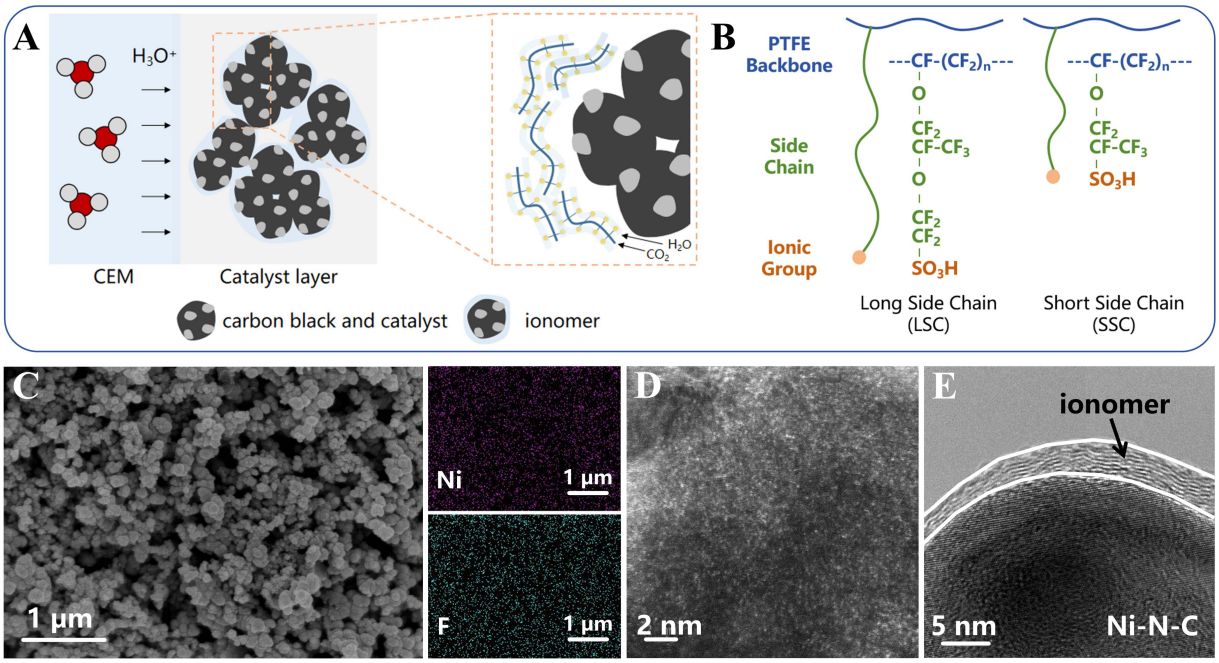

Figure 1. Morphology and structural characterization of the Ni-N-C catalyst. (A) Schematic illustration of ionomer and catalyst (red, gray, and yellow spheres correspond to oxygen atoms, hydrogen atoms, and sulfonic acid groups, respectively); (B) Chemical structure of PFSA ionomers; (C) SEM image and EDS mapping; (D) Aberration-corrected HAADF-STEM image; (E) TEM image.

influence of ionomer side chain structure, we selected two SSC ionomers (D72 and D79, both Aquivion-type) and two LSC ionomers (D520 and D521, both Nafion-type) for comparative study. As shown in Figure 1C, the as-prepared catalyst exhibits a spherical morphology typical of carbon black supports, with no obvious agglomeration and a uniform porous structure. Elemental mapping reveals distinct Ni and F signals, confirming the successful loading of Ni and ionomer onto the GDE surface. As shown in Figure 1D, HAADF-STEM images reveal numerous isolated bright spots on the carbon black, which correspond to uniformly dispersed single Ni atoms[26,27]. TEM images further demonstrate a distinct thin ionomer film, 2-3 nm thick, coating the catalyst surface [Figure 1E]. It is noteworthy that the SEM, TEM, and contact angle measurements of the D79- and D520-modified GDEs exhibited comparable results [Figure 1 and Supplementary Figures 4-6], indicating that the side chain structure exerts no significant influence on the electrode morphology or macroscopic wettability. Consequently, the subsequent differences in electrochemical performance cannot be attributed to these two factors.

CO_2 absorption-desorption tests were conducted on SSC-D79 and LSC-D520 to probe their microporous structures. As shown in Figure 2A-C, D79 exhibits a cumulative pore area of 3.36 $m^2 g^{-1}$, significantly higher than that of D520 (0.053 $m^2 g^{-1}$), with its micropores predominantly centered at 0.56 and 0.75 nm. The shorter side chains of D79 result in less dense packing of the polymer backbones during the formation of ion transport channels compared to their long side chain ionomers, thereby generating a greater number of smaller micropores at the nanoscale. This abundant microporous structure establishes a denser and more efficient ion transport network. Upon water uptake, these micropores form interconnected nanochannels, providing additional pathways for ion transport and enabling ions to migrate more smoothly without being isolated or blocked. These micropores not only provide additional pathways for ion transport but also serve as confinement sites for CO_2 adsorption, explaining the higher CO_2 uptake observed for D79. Studies have shown that the ionic conductivity of D79 is 2.5 times that of D520[28]. D79 exhibits a water uptake of 56.1%, markedly higher than the 14.2% observed for D520 [Figure 2D]. This advantage is attributable to its SSC architecture, which allows a greater number of hydrophilic sulfonic acid groups, key to water absorption, to

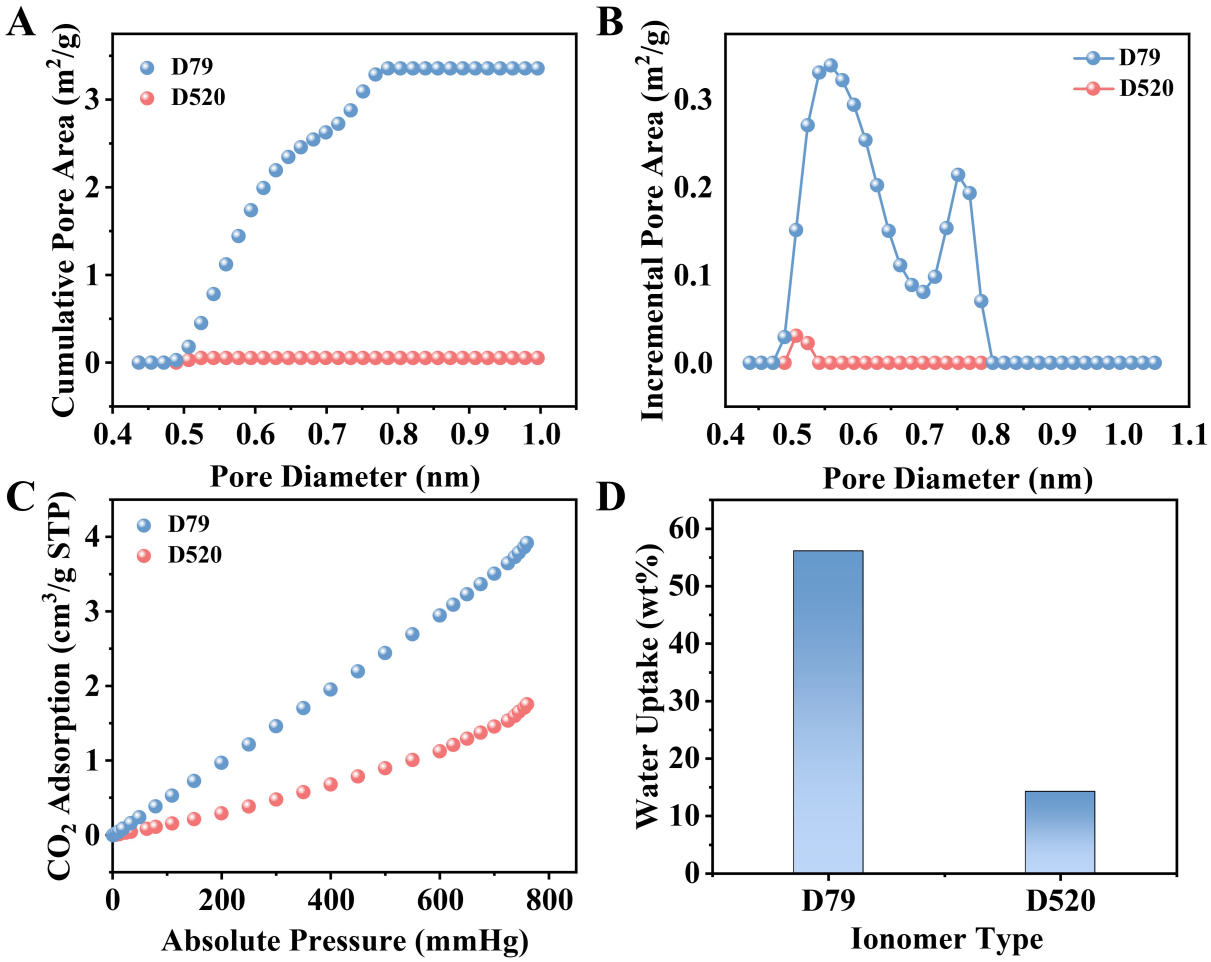

Figure 2. (A) Cumulative pore area, (B) Incremental pore area, (C) CO_2 adsorption curves and (D) Water uptake of ionomer membranes (D79 and D520).

be incorporated within the same polymer chain length, thereby facilitating the formation of a more favorable ionic network on the catalyst surface. It is worth noting that while D79 exhibits substantially higher water uptake than D520, the contact angles of the corresponding GDEs are similar [Supplementary Figure 4]. This apparent discrepancy arises because water uptake reflects the bulk absorption capacity of ionomer governed by the total sulfonic acid group density, whereas the contact angle probes the surface wettability of GDE, which is dominated by the hydrophobic PTFE backbone and carbon support rather than the sulfonic acid groups at the outermost surface layer.

CO_2 electroreduction performance in MEA electrolyzer

We first evaluated the performance of GDEs modified with SSC ionomers (D72, D79) and LSC ionomers (D520, D521) in the current density range of 100-400 mA cm^{-2}, which covers the typical operating window for acidic CO_2RR MEA systems reported in the literature. The results are presented in Figure 3, where both D72 and D79 maintained a CO selectivity of nearly 90% over a current density range of 100-400 mA cm^{-2} in 0.5 M K_2SO_4 electrolyte (pH 1, adjusted with H_2SO_4). At 400 mA cm^{-2}, D79 still achieved a FE_{CO} of 88.6%, while the LSC ionomers D520 and D521 exhibited FE_{CO} of 69.6% and 59.6%, respectively. The difference in FE_{CO} between D521 and D79 approached 30% [Supplementary Figure 7]. Meanwhile, D521 showed an FE_{H_2} of 38.3% at 400 mA cm^{-2}, indicating that the interfacial water structure formed by LSC ionomers fails to suppress water transport near the catalyst under high current densities, leading to a marked enhancement of

the competing HER. In addition, the cell voltages of D520 and D521 were generally 0.1-0.2 V higher than those of D72 and D79, which can be attributed to the higher ionic conductivity per unit mass of SSC ionomers. A control GDE containing only PTFE (without any ionomer) was also tested, delivering an FE_{CO} of merely 12.9% at 300 mA cm^{-2}. In the absence of hydrophilic sulfonic acid groups to regulate the hydrogen-bonding network near the catalyst, the high proton concentration under acidic conditions directly aggravated HER. Beyond the intrinsic properties of the ionomers, their interaction with the Nafion membrane also plays a critical role in determining the overall MEA performance. Both D79 and D520 are PFSA ionomers based on the same PTFE backbone, which ensures good compatibility at the catalyst layer-membrane interface and minimizes interfacial resistance. However, different side-chain structures result in distinct water uptake and proton conductivity, which can affect the hydration state at the interface. The higher water uptake and proton conductivity of D79 facilitate proton transport from the membrane to the catalyst layer, maintaining a sufficient proton supply for CO_2RR under high-current-density operation. At the same time, the dense sulfonic acid groups in D79 create a strongly hydrogen-bonded interfacial water network that suppresses HER from free water, achieving a desirable balance between proton availability and HER suppression. Based on the FE and cell voltage according to Faraday's law, we calculated the CO production rate and energy consumption for both D79-modified and D520-modified GDEs [Supplementary Table 2]. For the D79-modified GDE, the CO production rate increases from 1.81 mmol h^{-1} cm^{-2} at 100 mA cm^{-2} to 6.61 mmol h^{-1} cm^{-2} at 400 mA cm^{-2}, while the corresponding energy consumption ranges from 6.04 to 8.39 kWh kg^{-1} CO. In contrast, the D520-modified GDE achieves a maximum CO production rate of only 5.20 mmol h^{-1} cm^{-2} at 400 mA cm^{-2}, with a significantly higher energy consumption of 11.04 kWh kg^{-1} CO. The superior performance of D79 is attributed to its higher FE_{CO} and lower cell voltage, both of which originate from effective regulation of the interfacial water structure and enhanced ionic conductivity of the SSC ionomer. These results substantiate the superior energy efficiency of the SSC ionomer strategy, thereby corroborating its viability for practical acidic CO_2 electrolysis. The above results revealed that the performance gap between SSC and LSC ionomers widened substantially at current densities above 200 mA cm^{-2}, indicating that the influence of the interfacial water hydrogen-bonding network on electrochemical performance was more pronounced at high-current-density operation. This observation motivated us to extend testing to 500 mA cm^{-2} to further verify the advantages of the SSC ionomer under high-current-density conditions. Accordingly, we further evaluated the FE_{CO} of D79 and D520 at 500 mA cm^{-2}, with D79 maintaining a high FE_{CO} of 91.1% while D520 exhibited only 61.8%. Collectively, these results demonstrate that ionomers can modulate the interfacial water structure on the catalyst surface, thereby significantly influencing product selectivity. To evaluate the operational stability of the D79-modified GDE, long-term continuous electrolysis was performed at a constant current density of 100 mA cm^{-2} for 12 h in 0.05 M K_2SO_4 electrolyte (pH 1, adjusted with H_2SO_4) [Supplementary Figure 8], where a lower K^+ concentration was adopted to mitigate salt precipitation. As depicted, the FE_{CO} remained at approximately 83% for the first 3 h, and then gradually diminished to 79% by the end of the 12-h test. Meanwhile, the cell voltage exhibited a negligible increment from 3.08 to 3.11 V throughout the electrolysis period. These results collectively corroborate the good stability of the D79-modified GDE under sustained acidic CO_2 electrolysis. Finally, to verify the universality of the SSC ionomer strategy, we extended the investigation to Ag-based catalysts [Supplementary Figure 9]. Under identical testing conditions, the D79-modified Ag GDE delivered a FE_{CO} of 90.6% at a current density of 300 mA cm^{-2}, markedly surpassing that of the D520-modified Ag GDE (76.9%). This consistent performance enhancement across different catalytic systems substantiates the broad applicability of the SSC ionomer approach for acidic CO_2 electroreduction.

In-situ ATR-SEIRAS characterization of the interfacial water structure.

To elucidate the interfacial water structures of SSC and LSC ionomers, *in situ* ATR-SEIRAS measurements were conducted, with the results presented in Figure 4. The broad feature appearing between 3,000 and 3,800 cm^{-1} is attributed to the O-H stretching vibration mode, reflecting the unique hydrogen-bonding

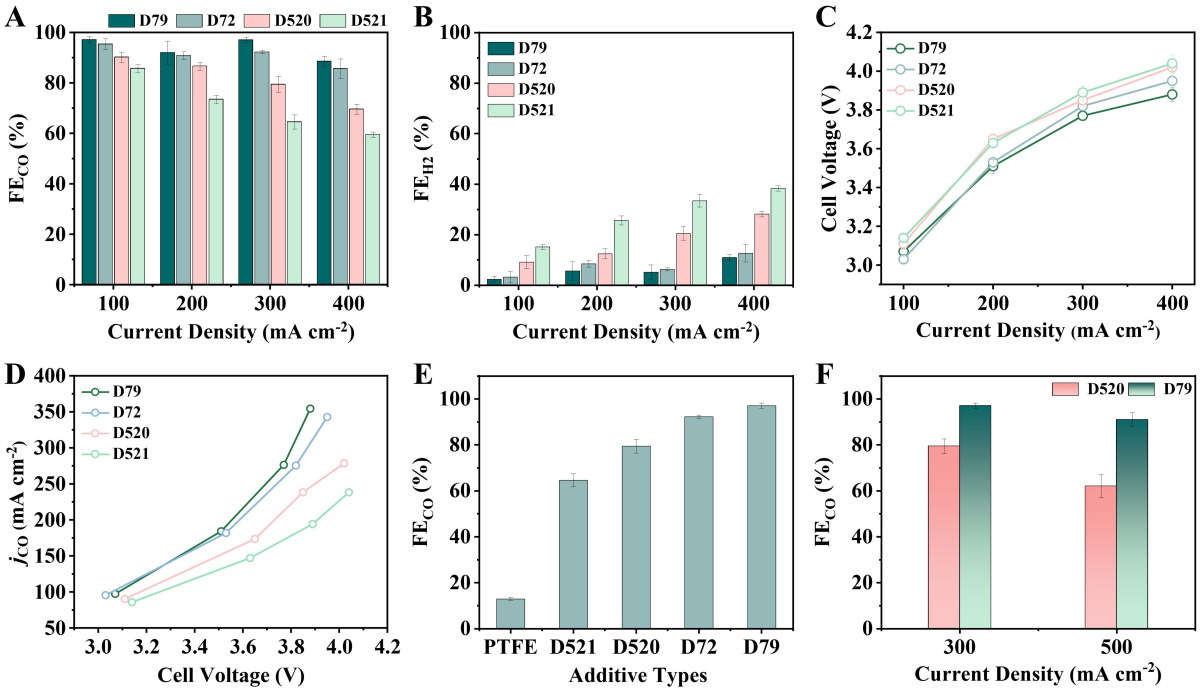

Figure 3. CO_2 electroreduction performance of GDEs with different ionomers. (A) FE_{CO}, (B) FE_{H2}, (C) Cell voltage, and (D) j_{CO} of GDEs with D72, D79, D520, and D521 at various current densities; (E) FE_{CO} of GDEs with different ionomers (D72, D79, D520, D521) at 300 mA cm^{-2}. The bar labeled PTFE represents a control GDE prepared without ionomer, using only PTFE as the binder. (F) FE_{CO} of GDEs with D79 and D520 at 500 mA cm^{-2}. All ionomer-to-catalyst ratios were fixed at 20 wt% (I/C = 0.25). Error bars represent the standard deviation from three independent measurements.

network formed by interfacial water[29]. Spectral deconvolution resolves this broad band into three distinct peaks centered at approximately 3,600, 3,380, and 3,250 cm^{-1}, which are characteristic of free water, weakly hydrogen-bonded water, and strongly hydrogen-bonded water, respectively[30]. In the spectra of GDEs modified with different side chain ionomers, absorption peaks corresponding to weakly hydrogen-bonded water (3,380 cm^{-1}) and strongly hydrogen-bonded water (3,250 cm^{-1}) were observed. Owing to the more densely packed sulfonate groups in SSC ionomers, they can form a more extensive and stronger hydrogen-bonding network. As shown in Figure 4A and C, with increasing applied potential, the content of strongly hydrogen-bonded interfacial water on the D79-modified GDE (SSC) gradually increased from 46.6% at -0.7 V *vs.* RHE to 60.5% at -1.7 V *vs.* RHE. This enhanced intermolecular hydrogen bonding is likely attributed to the intensified interfacial electric field upon potential application, which induces a more ordered dipole alignment of water molecules[31]. In contrast, for GDEs modified with LSC ionomers, the proportion of weakly hydrogen-bonded water consistently exceeded 60%, and the corresponding absorption peak gradually intensified with increasing potential [Figure 4B and D]. It is noteworthy that the absolute peak intensity for D79 showed minimal change with increasing potential, whereas for D520 it increased substantially. This difference arises because the SSC ionomer already forms a significant strongly hydrogen-bonded network at low potential due to its high sulfonic acid group density. The applied potential primarily drives water reorientation rather than increasing total water population. In contrast, the LSC ionomer interface is dominated by weakly hydrogen-bonded water, and the applied potential gradually induces both water accumulation and reorientation, resulting in more pronounced absolute intensity changes. When SSC ionomers induce the formation of a strongly hydrogen-bonded network, water molecules become anchored to specific lattice sites. This strong confinement increases the energy barrier for breaking hydrogen bonds, potentially hindering proton migration via the Grotthuss (hopping) mechanism. Consequently, proton transport may be forced to transition toward a vehicle mechanism, in which protons diffuse together with their hydration shells [Figure 4E and F]. This proposed transition would ultimately lead to a substantial

reduction in the interfacial proton flux[32], a scenario that is consistent with the observed increase in strongly hydrogen-bonded water and the concomitant suppression of the HER. Moreover, it is well established that water molecules exhibit a reorientation from H-up to H-down configurations when a negative potential is applied[33]. The distance between the catalyst and hydrogen atoms is governed by differences in the orientational reconfiguration behavior of water molecules. As shown in Figure 4G, a strong hydrogen-bonding network not only increases the catalyst-H distance but also more effectively immobilizes water molecules and H^+, preventing their approach to the vicinity of active sites and reducing water dissociation[34]. Consequently, the HER is significantly suppressed, which explains why the D79-modified GDE maintains a high CO selectivity even at high current densities.

Effect of ionomer on mass transfer

The catalyst/ionomer ratio within the catalyst layer significantly influences mass transport processes. An excessively low ionomer ratio exposes a larger active area to the acidic electrolyte, thereby promoting the HER. Conversely, an excessively high ionomer ratio impedes gaseous CO_2 transport [Figure 5A]. Moreover, elevated ionomer concentrations facilitate proton transport, thereby reducing CO selectivity. To investigate the impact of local CO_2 and proton transport modulated by the ionomer on electrochemical performance, we systematically varied the catalyst/ionomer ratio. The CO_2RR performance was evaluated across five different D79 loadings (5, 10, 20, 30, and 40 wt%). Supplementary Figure 10 reveals that the F content rises with increasing ionomer content, confirming that the prepared GDEs possess substantially different ionomer loadings. As shown in Figure 5B and Supplementary Figure 11, CO selectivity and cell voltage exhibited a volcano-type trend as the D79 ratio increased. The optimal performance was achieved at 20 wt% D79, yielding a FE_{CO} of 97.1% at 300 mA cm^{-2}. In contrast, at the same current density, the FE_{CO} was only 11.8% for the GDE with 5 wt% D79 and decreased from 97.1% to 62.5% when the D79 ratio was increased from 20 wt% to 40 wt%. This is because a high ionomer ratio impedes CO_2 diffusion, whereas a low ionomer ratio exacerbates HER by exposing active sites to the acidic environment. To investigate the underlying reasons for this phenomenon, the ECSA of GDEs with varying ionomer ratio was determined using the double-layer capacitance method [Supplementary Figure 12][35,36]. As shown in Figure 5C, the C_{dl} increased from 5.69 mF cm^{-2} at 5 wt% D79 to a maximum of 10.5 mF cm^{-2} at 20 wt% D79, then decreased to 6.48 mF cm^{-2} at 40 wt% D79. This indicates that the GDE with 20 wt% D79 possesses the optimal ECSA, which facilitates the formation of more three-phase reaction interfaces near the active sites, thereby promoting CO_2RR. EIS is a non-destructive analytical technique capable of real-time monitoring of charge transfer and mass transport processes in electrochemical systems[37,38]. As shown in Figure 5D, the GDE with 20 wt% D79 exhibited the lowest ohmic resistance of 16.9 Ω and the smallest charge transfer resistance of 13.3 Ω, suggesting that this ionomer ratio achieves an optimal balance between CO_2 transport and ion transport, establishing a stable three-phase reaction interface conducive to efficient CO_2RR. In summary, the experimental results demonstrate that precisely controlling the catalyst/ionomer ratio within the catalyst layer is critically important, as it profoundly influences local mass transport and overall electrochemical performance. Insufficient ionomer ratio fails to suppress the HER via the hydrogen-bonding network formed by the interfacial water structure, while excessive ionomer ratio hinders CO_2 transport. Optimizing this ratio is particularly essential in acidic electrolysis with high H^+ concentration to balance ionic transport and CO_2 diffusion at the interface, thereby achieving maximal CO selectivity.

By converting EIS data from the frequency domain to the time domain, the DRT can effectively resolve multiple processes with close time constants, thereby simplifying the interpretation of EIS results[39,40]. This method has been successfully applied to the diagnostic assessment of various electrochemical systems, including lithium-ion batteries, fuel cells, and water electrolyzers[41,42]. To elucidate the influence of ionomer content on CO_2 transport, DRT analysis was conducted[43,44]. On the basis of the characteristic frequency ranges and their responses to variations in ionomer loading, current density, and CO_2 partial pressure, the

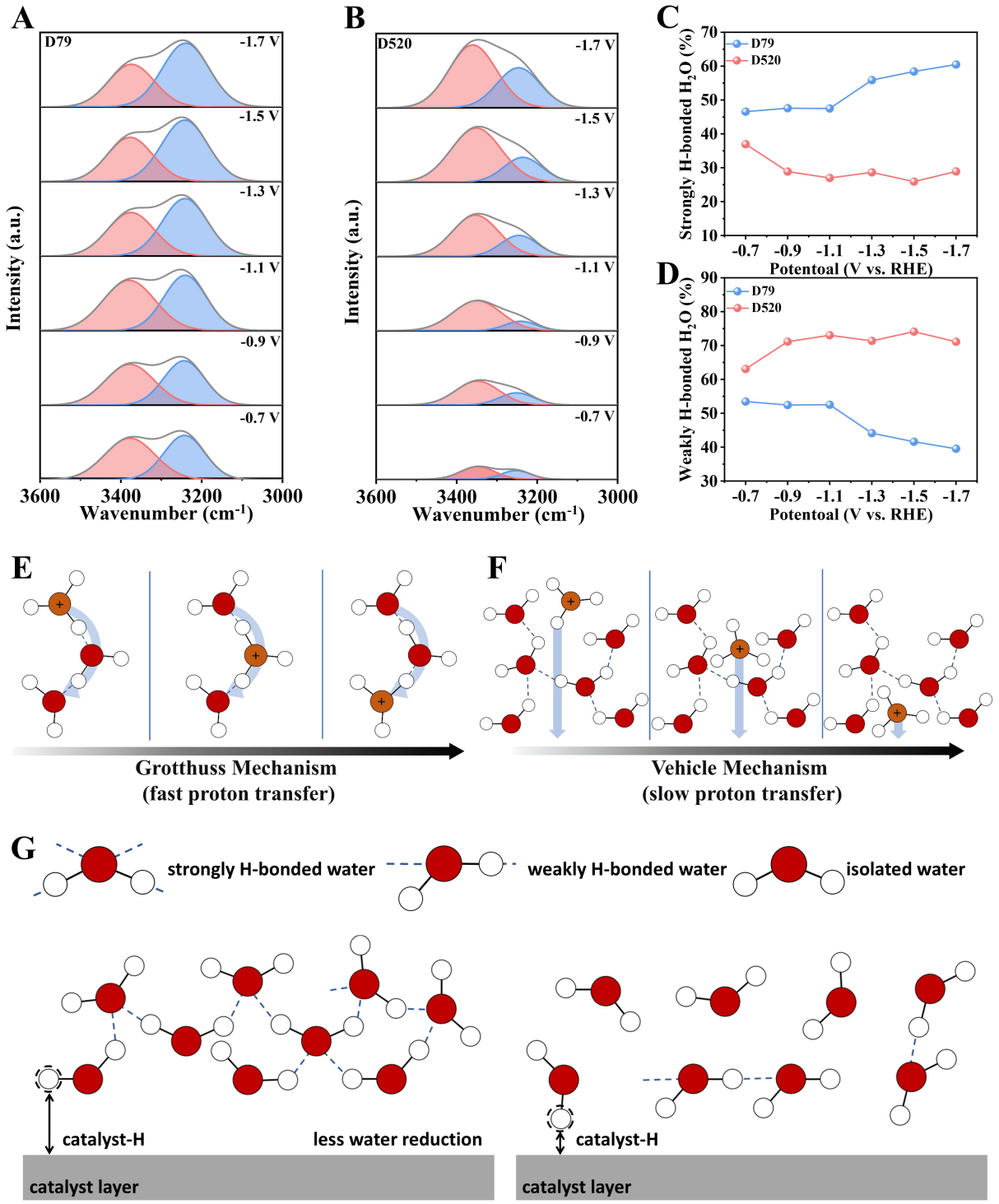

Figure 4. (A and B) Interfacial water structure probed by *in-situ* ATR-SEIRAS on GDEs with D79 and D520 (The peaks for weakly and strongly hydrogen-bonded water are shown in red and blue, respectively); (C and D) Normalized band intensities at ~3,250 and ~3,380 cm^{-1} for GDEs with D79 and D520; (E and F) Schematic diagram of the Grotthuss mechanism and the vehicle mechanism for proton transport; (G) Schematic diagram of strongly and weakly hydrogen bond networks. (Red and white spheres denote O and H atoms. Solid and dashed lines represent intramolecular O-H bonds and intermolecular O-H···O hydrogen bonds, respectively).

DRT peaks are systematically deconvoluted and assigned as follows: the high-frequency feature (1-10 kHz) is ascribed to ohmic and ionic transport resistance; the mid-frequency feature (10-200 Hz) is attributed to the charge transfer resistance associated with the CO_2RR; and the low-frequency feature (1-10 Hz) originates

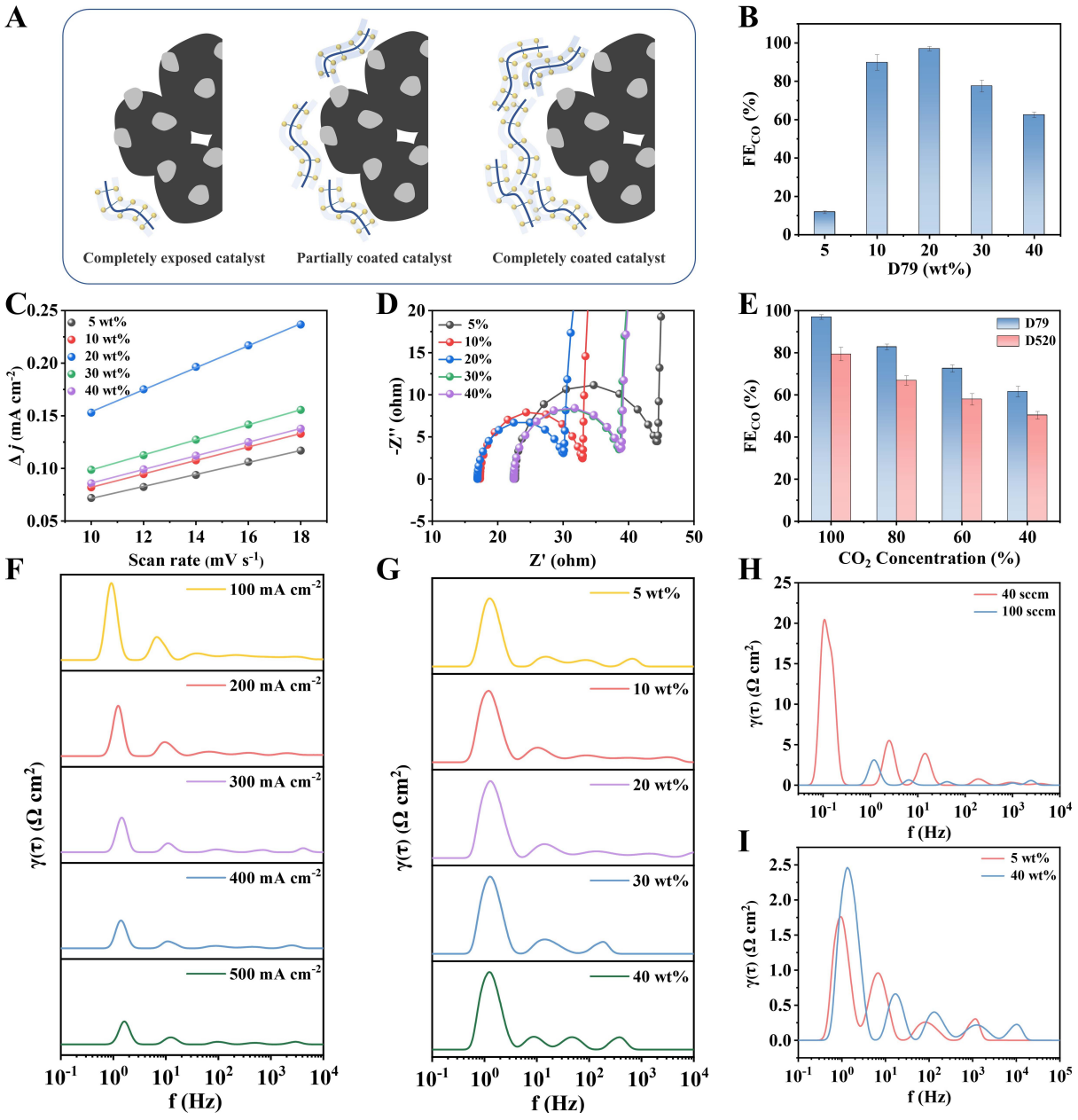

Figure 5. (A) Schematic illustration of the catalyst layer structure with varying ionomer ratio; (B) FE_{CO} of GDEs with varying ionomer ratio at 300 mA cm^{-2}; (C) ECSA and (D) EIS of GDEs with varying ionomer ratio; (E) FE_{CO} of GDEs with D79 and D520 at different CO_2 concentration; (F) DRT plot of GDE with 20 wt% D79 at 100-500 mA cm^{-2}; (G) DRT plot of GDE with varying ionomer ratio at 300 mA cm^{-2}; (H) DRT plot of GDE with 20 wt% D79 at varying flow rates at 300 mA cm^{-2}; (I) DRT plot of GDE with 5wt% D79 and 40wt% D79 at 300 mA cm^{-2}. Error bars represent the standard deviation from three independent measurements. Note that the x-axes in panels F-I are presented in logarithmic (Log10) scale.

from CO_2 mass transport limitations. Figure 5E demonstrates that the FE_{CO} declines as the CO_2 concentration is reduced, suggesting that CO_2 mass transport plays an important role in determining the electrochemical performance. As shown in Figure 5F, as the current density increases from 100 to 500 mA cm^{-2}, the CO_2 transport peak in the DRT spectra shifts to higher frequencies with a concurrent decrease in peak area. This behavior reflects a significant enhancement in mass transport within the MEA electrolyzer, where the substantial increase in CO_2 consumption at high current densities leads to a greater demand for CO_2 supply[45]. The effect of ionomer ratio on CO_2 transport was further investigated. As presented in Figure 5G, the CO_2 transport peak progressively increases with higher ionomer ratio. Reducing

the CO_2 flow rate enlarges the CO_2 transport peak [Figure 5H], indicating a marked rise in transport resistance, which would consequently lead to a decline in FE_{CO} with decreasing CO_2 concentration. A direct comparison between the 5 and 40 wt% GDEs [Figure 5I] reveals that increasing the ionomer ratio not only enlarges the CO_2 transport peak but also reduces the CO_2 reaction peak. This suggests that although a higher ionomer ratio increases CO_2 transport resistance, it simultaneously enhances CO_2RR kinetics by promoting the formation of a favorable interfacial water structure and the establishment of efficient ion transport pathways. Therefore, optimizing the ionomer ratio is essential to balance CO_2 transport and CO_2RR kinetics, which accounts for the highest FE_{CO} observed for the GDE with 20 wt% D79 in the performance tests shown in Figure 5B.

CONCLUSIONS

In summary, this study systematically investigated the influence of ionomer side chain on the interfacial microenvironment for CO_2RR in an acidic MEA electrolyzer. The SSC ionomer D79, characterized by densely packed sulfonic acid groups, exhibited a substantially higher micropore area (3.36 $m^2 g^{-1}$) than the LSC ionomer D520 (0.053 $m^2 g^{-1}$) and promoted more ordered dipole alignment of water molecules. *In situ* ATR-SEIRAS revealed that the SSC ionomer facilitates the formation of a strongly hydrogen-bonded interfacial water network (over 60% at -1.7 V *vs.* RHE), effectively reducing the proton flux and inhibiting water dissociation, thereby suppressing the competitive HER. Consequently, the GDE with D79 maintained a high FE_{CO} of 91.1% at 500 mA cm^{-2}, substantially outperforming the LSC-D520 (61.8%). Furthermore, optimization of the ionomer content (20 wt% D79) balanced CO_2 transport and reaction kinetics. This work demonstrates that the ionomer side chain effectively regulates the interfacial water hydrogen-bond network and alters the proton transport pathway, offering critical insights into the engineering of microenvironments for acidic CO_2RR.

DECLARATIONS

Authors' contributions

Made substantial contributions to conception and design of the study and performed data acquisition, analysis, and interpretation: Kang, Z.; Zhang, M.; Wang, Y.; Fu, Q.
Provided administrative, technical, and material support: Liao, Q.; Zhu, X

Availability of data and materials

The original contributions presented in this study are included in the article/Supplementary Materials. Further inquiries can be directed to the corresponding authors.

AI and AI-assisted tools statement

Not applicable.

Financial support and sponsorship

The authors highly appreciate the financial support from the National Natural and Science Foundation of China (No. 52394202, 52476056, 52301232) and the Natural Science Foundation of Chongqing Province (2024NSCQ-MSX1109).

Conflicts of interest

All authors declared that there are no conflicts of interest.

Ethical approval and consent to participate

Not applicable.

Consent for publication

Not applicable.

Supplementary Materials

Supplementary Materials

REFERENCES

1. Li, L.; Chen, J.; Mosali, V. S. S.; et al. Hydrophobicity graded gas diffusion layer for stable electrochemical reduction of CO_2. *Angew. Chem. Int. Ed.* **2022**, *61*, e202208534. DOI PubMed PMC
2. Nitopi, S.; Bertheussen, E.; Scott, S. B.; et al. Progress and perspectives of electrochemical CO_2 reduction on copper in aqueous electrolyte. *Chem. Rev.* **2019**, *119*, 7610-72. DOI
3. Luna P, Hahn C, Higgins D, Jaffer SA, Jaramillo TF, Sargent EH. What would it take for renewably powered electrosynthesis to displace petrochemical processes? *Science* **2019**, *364*, eaav3506. DOI PubMed
4. Jin, J.; Wicks, J.; Min, Q.; et al. Constrained C2 adsorbate orientation enables CO-to-acetate electroreduction. *Nature* **2023**, *617*, 724-9. DOI
5. Ha, T. H.; Kim, J.; Choi, H.; Oh, J. Selective zero-gap CO_2 reduction in acid. *ACS. Energy. Lett.* **2024**, *9*, 4835-42. DOI
6. Wang, X.; Li, P.; Tam, J.; et al. Efficient CO and acrolein co-production via paired electrolysis. *Nat. Sustain.* **2024**, *7*, 931-7. DOI
7. Goyal, A.; Marcandalli, G.; Mints, V. A.; Koper, M. T. M. Competition between CO_2 reduction and hydrogen evolution on a gold electrode under well-defined mass transport conditions. *J. Am. Chem. Soc.* **2020**, *142*, 4154-61. DOI PubMed PMC
8. Xie, Y.; Ou, P.; Wang, X.; et al. High carbon utilization in CO_2 reduction to multi-carbon products in acidic media. *Nat. Catal.* **2022**, *5*, 564-70. DOI
9. Monteiro, M. C. O.; Philips, M. F.; Schouten, K. J. P.; Koper, M. T. M. Efficiency and selectivity of CO_2 reduction to CO on gold gas diffusion electrodes in acidic media. *Nat. Commun.* **2021**, *12*, 4943. DOI PubMed PMC
10. Wu, W.; Wang, Y. The role of protons in CO_2 reduction on gold under acidic conditions. *J. Am. Chem. Soc.* **2025**, *147*, 11662-6. DOI
11. Song, Y.; Musgrave, C. B.; Su, J.; et al. Efficient CO_2-to-methanol electrocatalysis in acidic media via microenvironment-tuned cobalt phthalocyanine. *Nat. Nanotechnol.* **2025**, *21*, 78-86. DOI
12. Zhu, Y.; Tian, P.; Jiang, H.; et al. Synergistic effect of platinum single atoms and nanoclusters boosting electrocatalytic hydrogen evolution. *CCS. Chem.* **2021**, *3*, 2539-47. DOI
13. Cheng, Y.; Li, Q.; Salaman, M. I. B.; et al. Microenvironment tailoring for electrocatalytic CO_2 reduction: effects of interfacial structure on controlling activity and selectivity. *J. Am. Chem. Soc.* **2025**, *147*, 12438-48. DOI PubMed PMC
14. Xu, Z.; Zhang, X.; Wang, Q. In situ spectroscopy study of $PrO_{1.83}$/CuO interface in CO_2 electroreduction: microenvironment regulation and enhancement mechanism. *Appl. Catal. B. Environ. Energy.* **2026**, *385*, 126261. DOI
15. Zhang, Z.; Wang, T.; Cai, Y.; et al. Probing electrolyte effects on cation-enhanced CO_2 reduction on copper in acidic media. *Nat. Catal.* **2024**, *7*, 807-17. DOI
16. Fan, J.; Pan, B.; Wu, J.; et al. Immobilized tetraalkylammonium cations enable metal-free CO_2 electroreduction in acid and pure water. *Angew. Chem. Int. Ed.* **2024**, *63*, e202317828. DOI
17. Li, G.; Huang, L.; Wei, C.; et al. Backbone engineering of polymeric catalysts for high-performance CO_2 reduction in bipolar membrane zero-gap electrolyzer. *Angew. Chem. Int. Ed.* **2024**, *136*, e202400414. DOI
18. Wu, B.; Wang, B.; Cai, B.; et al. A solid-state electrolyte facilitates acidic CO_2 electrolysis without alkali metal cations by regulating proton transport. *J. Am. Chem. Soc.* **2024**, *146*, 29801-9. DOI
19. Xing, M.; Zhang, H.; Kang, Z.; Zhang, M.; Zhu, X.; Fu, Q. High-performance CO_2 electrolysis in membrane electrode assemblies: the role of non-alkali cations. *Chem. Sci.* **2026**, Online ahead of print. DOI PubMed PMC
20. Yang, Y.; Wang, J.; Shi, Y.; et al. Decoupling product selectivity in electrocatalytic CO_2 reduction by steering the interfacial water structure. *J. Am. Chem. Soc.* **2026**, *148*, 11284-95. DOI
21. Mi, Z.; Wang, T.; Xiao, L.; Wang, G.; Zhuang, L. Catalytic peculiarity of alkali metal cation-free electrode/polyelectrolyte interfaces toward CO_2 reduction. *J. Am. Chem. Soc.* **2024**, *146*, 17377-83. DOI
22. Krivina, R. A.; Lindquist, G. A.; Yang, M. C.; et al. Three-electrode study of electrochemical ionomer degradation relevant to anion-exchange-membrane water electrolyzers. *ACS. Appl. Mater. Interfaces.* **2022**, *14*, 18261-74. DOI
23. Liang, Z.; Chen, W.; Liu, J.; et al. FT-IR study of the microstructure of Nafion® membrane. *J. Membr. Sci.* **2004**, *233*, 39-44. DOI
24. Bard, A. J.; Faulkner, L. R.; White, H. S. Electrochemical methods: fundamentals and applications, 3rd Edition. John Wiley & Sons; 2022. Available from: https://www.wiley.com/en-cn/shop/general-chemistry/electrochemical-methods-fundamentals-and-applications-3rd-edition-p-9781119334057 [Last accessed on 30 Jul 2026].

25. Sun, J.; Wu, B.; Wang, Z.; et al. Rational catalyst layer design enables tailored transport channels for efficient CO_2 electrochemical reduction to multi-carbon products. *Energy. Environ. Sci.* **2025**, *18*, 1027-37. DOI
26. Zhao, C.; Wang, Y.; Li, Z.; et al. Solid-diffusion synthesis of single-atom catalysts directly from bulk metal for efficient CO_2 reduction. *Joule* **2019**, *3*, 584-94. DOI
27. Zhang, Q.; Tan, X.; Bedford, N. M.; et al. Direct insights into the role of epoxy groups on cobalt sites for acidic H_2O_2 production. *Nat. Commun.* **2020**, *11*, 4181. DOI PubMed PMC
28. Ponomar, M. A.; Kislyi, A. G.; Kozmai, A. E.; et al. Characterization and process-structure-properties modeling of ion-exchange membranes of Aquivion®-type based on perfluorosulphonic acid ionomer with short side chains. *Int. J. Hydrogen. Energy.* **2025**, *115*, 170-85. DOI
29. Schaefer, J.; Backus, E. H. G.; Nagata, Y.; Bonn, M. Both inter- and intramolecular coupling of O-H groups determine the vibrational response of the water/air interface. *J. Phys. Chem. Lett.* **2016**, *7*, 4591-5. DOI PubMed
30. Rao, R. R.; Huang, B.; Katayama, Y.; et al. pH- and cation-dependent water oxidation on rutile RuO_2(110). *J. Phys. Chem. C.* **2021**, *125*, 8195-207. DOI
31. Despa, F.; Fernández, A.; Berry, R. S. Dielectric modulation of biological water. *Phys. Rev. Lett.* **2004**, *93*, 228104. DOI PubMed
32. Kharod, R. A.; Andrews, J. L.; Dincă, M. Teaching metal-organic frameworks to conduct: ion and electron transport in metal-organic frameworks. *Ann. Rev. Mater. Res.* **2022**, *52*, 103-28. DOI
33. Li, C.; Le, J.; Wang, Y.; et al. In situ probing electrified interfacial water structures at atomically flat surfaces. *Nat. Mater.* **2019**, *18*, 697-701. DOI
34. Wang, Y.; Zhang, J.; Zhao, J.; et al. Strong hydrogen-bonded interfacial water inhibiting hydrogen evolution kinetics to promote electrochemical CO_2 reduction to C_{2+}. *ACS. Catal.* **2024**, *14*, 3457-65. DOI
35. Xing, Z.; Hu, L.; Ripatti, D. S.; Hu, X.; Feng, X. Enhancing carbon dioxide gas-diffusion electrolysis by creating a hydrophobic catalyst microenvironment. *Nat. Commun.* **2021**, *12*, 136. DOI PubMed PMC
36. Kwon, W.; Kim, J.; Rhee, S. A new equivalent circuit model for porous carbon electrodes in charge transfer reaction of iodide/triiodide redox couples. *Electrochim. Acta.* **2012**, *68*, 110-3. DOI
37. Rezaei Niya, S. M.; Hoorfar, M. Study of proton exchange membrane fuel cells using electrochemical impedance spectroscopy technique - A review. *J. Power. Sources.* **2013**, *240*, 281-93. DOI
38. Garcia-navarro, J.; Schulze, M.; Friedrich, K. Measuring and modeling mass transport losses in proton exchange membrane water electrolyzers using electrochemical impedance spectroscopy. *J. Power. Sources.* **2019**, *431*, 189-204. DOI
39. Li, Y.; Jiang, Y.; Dang, J.; et al. Application of distribution of relaxation times method in polymer electrolyte membrane water electrolyzer. *Chem. Eng. J.* **2023**, *451*, 138327. DOI
40. Schmidt, J. P.; Berg, P.; Schönleber, M.; Weber, A.; Ivers-Tiffée, E. The distribution of relaxation times as basis for generalized time-domain models for Li-ion batteries. *J. Power. Sources.* **2013**, *221*, 70-7. DOI
41. Iurilli, P.; Brivio, C.; Wood, V. Detection of lithium-ion cells' degradation through deconvolution of electrochemical impedance spectroscopy with distribution of relaxation time. *Energy. Technol.* **2022**, *10*, 2200547. DOI
42. Giesbrecht, P. K.; Freund, M. S. Investigation of water oxidation at IrO_2 electrodes in nafion-based membrane electrode assemblies using impedance spectroscopy and distribution of relaxation times analysis. *J. Phys. Chem. C.* **2022**, *126*, 17844-61. DOI
43. Chen, L.; Chen, J.; Chen, J.; Xi, S.; Stewart, J.; Wang, L. Operando interfacial diagnosis in MEA reactors for energy-efficient CO reduction at high rate. *Joule* **2026**, *10*, 102361. DOI
44. Chen, Q.; Kube, A.; Kopljar, D.; Friedrich, K. A. Advanced impedance analysis for performance degradation during low-temperature CO_2 electroreduction. *ACS. Energy. Lett.* **2024**, *9*, 6096-103. DOI
45. Qu, Y.; Yang, K.; Li, W.; et al. Operando diagnosis of MEA-type CO_2 electrolyzer via distribution of relaxation times analysis. *ACS. Energy. Lett.* **2024**, *9*, 3042-8. DOI